PHYSICAL REVIEW RESEARCH **6**, L012008 (2024)

Letter

Measurements of Penning-Malmberg trap patch potentials and associated performance degradation

C. J. Baker,[1] W. Bertsche,[2,3] A. Capra,[4] C. L. Cesar,[5] M. Charlton,[1] A. Christensen,[6,*] R. Collister,[4] A. Cridland Mathad,[1] S. Eriksson,[1] A. Evans,[7] N. Evetts,[7] J. Fajans,[6,†] T. Friesen,[8] M. C. Fujiwara,[4] D. R. Gill,[4] P. Grandemange,[4] P. Granum,[9] J. S. Hangst,[9] M. E. Hayden,[10] D. Hodgkinson,[2] E. D. Hunter,[6] C. A. Isaac,[1] M. A. Johnson,[2] J. Jones,[1] S. A. Jones,[1] S. Jonsell,[11] A. Khramov,[4] L. Kurchaninov,[4] H. Landsberger,[6] N. Madsen,[1] D. Maxwell,[1] J. T. K. McKenna,[9,4] S. Menary,[12] T. Momose,[7] P. S. Mullan,[1] J. J. Munich,[10] K. Olchanski,[4] A. Olin,[4,13] J. Peszka,[1] A. Powell,[1,8] P. Pusa,[14] C.Ø. Rasmussen,[15] F. Robicheaux,[16] R. L. Sacramento,[5] M. Sameed,[1] E. Sarid,[17] D. M. Silveira,[5] C. So,[8] G. Stutter,[9] T. D. Tharp,[18] R. I. Thompson,[8] C. Torkzaban,[6] D. P. van der Werf,[1] E. Ward,[6] and J. S. Wurtele[6]
(ALPHA Collaboration)

[1]*Department of Physics, Faculty of Science and Engineering, Swansea University, Swansea SA2 8PP, United Kingdom*
[2]*School of Physics and Astronomy, University of Manchester, Manchester M13 9PL, United Kingdom*
[3]*Cockcroft Institute, Sci-Tech Daresbury, Warrington WA4 4AD, United Kingdom*
[4]*TRIUMF, 4004 Wesbrook Mall, Vancouver BC, V6T 2A3, Canada*
[5]*Instituto de Física, Universidade Federal do Rio de Janeiro, Rio de Janeiro 21941-972, Brazil*
[6]*Department of Physics, University of California at Berkeley, Berkeley, California 94720-7300, USA*
[7]*Department of Physics and Astronomy, University of British Columbia, Vancouver BC, V6T 1Z1, Canada*
[8]*Department of Physics and Astronomy, University of Calgary, Calgary AB, T2N 1N4, Canada*
[9]*Department of Physics and Astronomy, Aarhus University, DK-8000 Aarhus C, Denmark*
[10]*Department of Physics, Simon Fraser University, Burnaby BC, V5A 1S6, Canada*
[11]*Department of Physics, Stockholm University, SE-10691, Stockholm, Sweden*
[12]*Department of Physics and Astronomy, York University, Toronto, ON M3J 1P3, Canada*
[13]*Department of Physics and Astronomy, University of Victoria, Victoria BC, V8P 5C2, Canada*
[14]*Department of Physics, University of Liverpool, Liverpool L69 7ZE, United Kingdom*
[15]*CERN, Experimental Physics Department, CH-1211 Genève 23, Switzerland*
[16]*Department of Physics and Astronomy, Purdue University, West Lafayette, Indiana 47907, USA*
[17]*Soreq NRC, Yavne, 81800, Israel*
[18]*Physics Department, Marquette University, P.O. Box 1881,Milwaukee, Wisconsin 53201-1881, USA*

(Received 5 July 2022; accepted 23 October 2023; published 16 January 2024)

Antiprotons created by laser ionization of antihydrogen are observed to rapidly escape the ALPHA trap. Further, positron plasmas heat more quickly after the trap is illuminated by laser light for several hours. These phenomena can be caused by patch potentials—variations in the electrical potential along metal surfaces. A simple model of the effects of patch potentials explains the particle loss, and an experimental technique using trapped electrons is developed for measuring the electric field produced by the patch potentials. The model is validated by controlled experiments and simulations.

DOI: 10.1103/PhysRevResearch.6.L012008

Due to surface contamination, grain boundaries, etc., the surfaces of metals are not generally perfect equipotentials [1–8]. The resulting forces between macroscopic objects pose challenges to measurements on free-falling test masses in satellites [9–11], and to measurements of the Casimir force [12–16]. The forces due to patch potentials on charged particles are a significant source of error in the measurement of those particles' acceleration due to gravity [17–19]. Additionally, these forces have been shown to move trapped ions off center in Paul traps [7,20] and to adversely affect measurements in Penning traps [18,21,22]. Here we introduce a technique to measure the electric field due to patch potentials in a cryogenic Penning-Malmberg trap; we find that lasers can change patch potentials, but only while the trap remains cold. We show that patch potentials influence both the orbits of antiprotons and the temperatures of positron plasmas.

The ALPHA experiment produces trapped antihydrogen by mixing positron and antiproton nonneutral plasmas in the center of a combined magnetic minimum and Penning-Malmberg trap [23–25]. The plasmas are axially confined and controlled by manipulating the potentials on cylindrical electrodes and radially confined by an external solenoid which creates a constant $B = 1\,\mathrm{T}$ axial magnetic field (see Fig. 1).

In the course of a spectroscopy experiment [26,27], laser ionization of trapped antihydrogen atoms leaves antiprotons

---

[*] a.c@berkeley.edu
[†] joel@physics.berkeley.edu

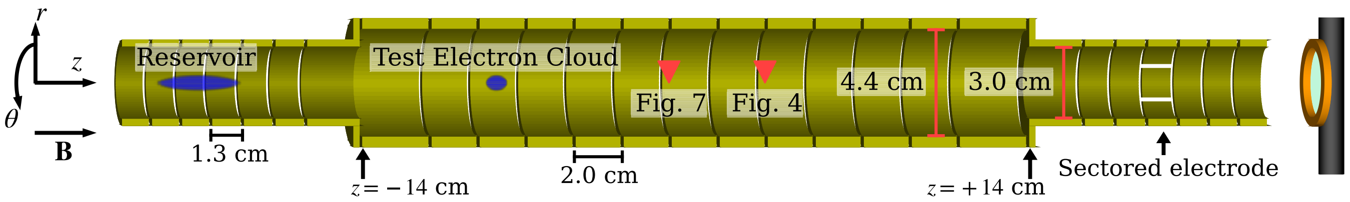

FIG. 1. The ALPHA-2 Penning-Malmberg trap. On the right is the microchannel plate (MCP)/phosphor screen/CCD camera detector. The electrodes are to scale, but the sizes of the electron reservoir and test electron cloud have been exaggerated, and the MCP is further away than depicted. Red triangles show the locations where the data for Figs. 4 and 7 were taken.

with a recoil energy of $\mathcal{O}(1\,\text{meV})$. Simulations of antiproton trajectories in the trap, including all reasonable magnetic field errors, showed that antiprotons should be confined in potential wells resulting from voltage offsets on the electrode amplifiers $[\mathcal{O}(10\,\text{mV})]$. However, we know from a surrounding silicon vertex detector that these antiprotons hit the trap wall and annihilate [27]. Further, this happens quickly; the detector signals become consistent with the cosmic ray background within 40 ms. This agrees with the behavior of antiproton plasmas in similar fields, which annihilate in a time $T \approx 20$ ms. In deeper potential wells $[\mathcal{O}(10\,\text{V})]$, the antiprotons remain confined for hours [28,29].

Here, we consider whether patch potentials combined with shallow electrostatic wells could explain the antiproton loss. We postulate that the lowest order term (in r) which satisfies the Laplace equation but cannot be generated by the symmetric electrodes is $\Phi_\text{P}(r,\theta,z) = \varepsilon r\cos(\theta)$, where ε is the transverse electric field magnitude. If the resulting field is stronger than the trapping potential, antiprotons will $\mathbf{E}\times\mathbf{B}$ drift to the trap wall (radius $R_\text{w} = 2.2$ cm) and annihilate. A patch field of $\varepsilon = BR_\text{w}/T = \mathcal{O}(10\,\text{mV/cm})$ is compatible with the measured annihilation time.

This field is consistent with Refs. [17,30], which find centimeter-scale potential variations along metallic surfaces of order 1–100 mV depending on the metal, coating, and cleaning method. Our gold-plated aluminum electrodes are cleaned in an acetone ultrasonic bath followed by an ethanol one. Previous authors have reported improved patch potentials after gold plating [31,32], and significant improvements are reported from colloidal graphite coating [30,31]. However, later we will speculate that a component of our patch fields is due to charges resting on cryopumped gas; there is no guarantee that any of these methods can prevent this kind of patch potential.

For small (r,z), the trapping potential for antiprotons can be approximated by $\Phi_\text{T}(r,\theta,z) = -k_2(z^2 - r^2/2) + \cdots$, where k_2 is the trap depth constant. The associated radial electric field will cause an off-axis charged particle to $\mathbf{E}\times\mathbf{B}$ drift in a circular "magnetron" orbit of angular frequency $\omega_r \approx -k_2/B$ centered around the trap axis. With a patch field, the orbit center will be displaced [33–35] from the trap axis by a distance $\delta = \varepsilon/k_2$ [36]. When $\delta \ll R_\text{w}$, this approximation is accurate because the scale factor suppressing higher order terms in Φ_T and Φ_P is R_w, even if the sizes of potential variations on the trap wall are smaller. When an antiproton nears the trap wall, this model is only an order of magnitude estimate. In ALPHA's laser experiments, the $1/k_2$ values created by the voltage offsets are $\mathcal{O}(1\,\text{cm}^2/\text{mV})$, so δ would be equal to the trap wall radius for ε of order 2 mV/cm.

To illustrate the loss process and to inform our experimental strategy, we simulated the motion of antiprotons in a realistic trapping potential calculated from the trap electrodes and a patch potential created by long strips (10 cm) of positive and negative voltage perturbations on the top and bottom of the trap, respectively (see Fig. 2). The simulation starts with a large k_2 so that the trap is deep and the antiproton is released from the center with 1 meV of kinetic energy. The parameter k_2 is then reduced adiabatically. The antiproton executes a small magnetron orbit, which moves off axis as k_2 decreases. The antiproton also oscillates axially; the range of this motion is small compared to R_w, so the trapping potential is approximately harmonic in z. Figure 2 plots the resulting magnetron center as a function of $1/k_2$.

For sufficiently shallow trapping potentials, the magnetron center departs from the simplistic value $\delta = \varepsilon/k_2$ because both the trapping and patch potentials deviate from their leading order estimates. An antiproton's $\mathbf{E}\times\mathbf{B}$ motion in the transverse plane causes it to orbit a potential energy maximum [33,37] and to move toward negatively charged patches. These transverse maxima are plotted in Fig. 2, and they agree with the simulation. For this particular combination of trapping and patch potentials, the maximum vanishes after the antiproton is pushed to $0.52R_\text{w}$, and the antiproton is no longer confined.

In the laser experiments, k_2 is held constant, not decreased as in the simulation. Nonetheless, an antiproton created and released from near the trap center will orbit its magnetron center [34,35], and will hit the wall if the center is sufficiently

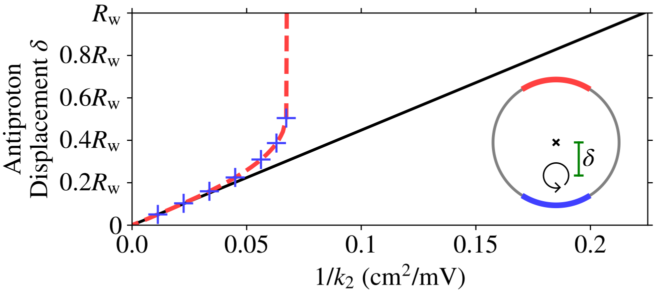

FIG. 2. Antiproton magnetron center displacements δ as a function of the inverse well constant $1/k_2$ found by trajectory simulations (dashed red line) and linear theory (black line). The patch field ε is 10 mV/cm. The blue plus (+) symbols show the radial positions of the (r,θ) potential energy maxima. The inset cartoon of a trap cross section illustrates an antiproton's $\mathbf{E}\times\mathbf{B}$ motion at fixed k_2 showing how δ is defined. The red and blue (top and bottom) arcs represent positive and negative voltage perturbations respectively.

far from the trap axis. Thus, an antiproton will hit the wall when $1/k_2$ is of order $1\,\mathrm{cm}^2/\mathrm{mV}$ and $\varepsilon = 10\,\mathrm{mV/cm}$; the resulting linear estimate puts the magnetron center beyond the trap wall.

Simply calculating that a small patch field could cause antiproton loss does not establish that patch fields are actually present and the source of this loss. Consequently, we developed an experimental technique using electron plasmas to measure the magnitude of patch fields ε. In brief, we vary the trap depth constant k_2 and measure how far charges move off axis. In more detail, the SDREVC (strong drive regime evaporative cooling) plasma stabilization technique [38] is used to prepare an electron plasma "reservoir" of ∼20 million electrons. Next, the electrode potentials are manipulated to sequentially extract small "test" electron clouds of ∼10 thousand electrons and radius ∼0.1 mm [39–41]. The clouds are then moved axially to a desired measurement location, where they are confined in the center of an electrode by applying a positive voltage to that electrode and grounding the surrounding ones. These manipulations leave them with an unavoidable magnetron orbit of radius ∼0.3 mm. The clouds have a temperature of $\mathcal{O}(300\,\mathrm{K})$. A grid based numerical equilibrium solver [42–44] finds that their diameter is between one and five Debye lengths, and their length ranges between 40 and 100 Debye lengths as the trap depth is varied, so the clouds do not exhibit complete Debye shielding. As a cloud is moved through the trap, it remains cohesive because its charge produces an internal electric field that induces a rotation at frequency $\mathcal{O}(200\,\mathrm{kHz})$ [45,46]. This electric field does not influence the bulk movement of the cloud, because an object cannot exert a net force on itself.

Next, we make the potential well shallower by decreasing the voltage on the confining electrode, thereby decreasing k_2 to a minimum value that we will define as k_{2m}. This process leaves the cloud in a magnetron orbit centered around the off-axis position $\delta = \varepsilon/k_{2m}$. If k_2 is changed slowly, the area of the magnetron orbit will be adiabatically conserved [47,48] and remain small. An adiabatic change requires that $d\delta/dt$ be much smaller than the $\mathbf{E}\times\mathbf{B}$ drift velocity. This drift velocity changes by several orders of magnitude as the electrode voltage is decreased from 70 V to 0.1–2 V. The adiabatic error is suppressed by using a twice differentiable, slowly changing function to vary k_2 [48–51].

After k_2 is decreased to k_{2m}, we restore k_2 to its original value quickly enough that the cloud does not significantly move. Since k_2 is now much larger than k_{2m}, the new orbital center is the trap axis, so the cloud is left in a large magnetron orbit with approximate radius ε/k_{2m}, but with a random variation Δr proportional to the radius of the initial magnetron orbit. We then wait 0.1 s during which the clouds complete a few thousand of these large orbits.

After this, we determine each cloud's location by releasing it toward the MCP detector (see Fig. 1). As the electrons move to the MCP, they follow magnetic field lines, which diverge by a factor of $\mathcal{R}_B \approx 10$, because the magnetic field at the MCP is about 1/100 that of the trap interior. The cloud centers are recorded in plots like Fig. 3. For identical electrode manipulations, the initial variations in the magnetron radii for each cloud cause variations in the total azimuthal angle subtended by magnetron motion θ_s, so together the cloud centers trace a spiral. The adiabatic decrease of k_2 to k_{2m} is required for observing this spiral (see Fig. 3).

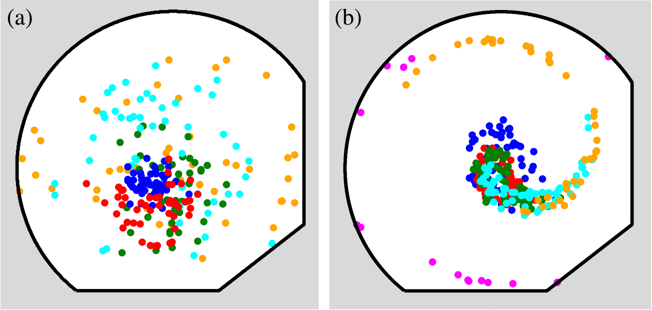

FIG. 3. Each dot represents the center of a cloud seen on the MCP after (a) a nonadiabatic and (b) an adiabatic decrease of k_2 to k_{2m}. The colors indicate the value of k_{2m} used for each cloud: 2.0κ (blue), 1.2κ (red), 1.0κ (green), 0.7κ (cyan), 0.5κ (orange), and 0.3κ (fuchsia); $\kappa = 87\,\mathrm{mV/cm}^2$. The black perimeter is the optical system aperture, which is about 4 cm wide.

The angle variations are due to the variation in ω_r with r. The dependence comes from higher order terms in the trapping potential:

$$\Phi_\mathrm{T} = -k_2\left(z^2 - \frac{1}{2}r^2\right) + k_3\left(z^3 - \frac{3}{2}zr^2\right) + k_4\left(z^4 - 3z^2r^2 + \frac{3}{8}r^4\right) + \cdots . \quad (1)$$

The third order term gives rise to an r dependent z equilibrium $\langle z\rangle = -3k_3r^2/(4k_2)$. To leading order, the angular frequency is given by

$$\omega_r(r) = -\frac{k_2}{B} + 6\frac{k_4\langle z^2\rangle}{B} - \left(\frac{9}{4}\frac{k_3^2}{k_2B} + \frac{3}{2}\frac{k_4}{B}\right)r^2 + \cdots , \quad (2)$$

where $\langle z^2\rangle$ is the average z^2 value for the cloud particles. The variation in ω_r due to Δr leads to a variation in the subtended angle on the order of one revolution after 0.1 s.

We measure ε by fitting a probability distribution to a dataset that employs multiple k_{2m} values. Figure 4 shows an example with 360 total data points evenly distributed between six different k_{2m} values. The distribution depends on six fit parameters: the angle θ_0 and proportionality constant k_θ for the spiral $\theta_s(r) = \theta_0 + k_\theta r^2$, the patch field ε, the variability of the initial cloud positions Δr, and the x and y position of the center of the trap as seen on the MCP screen. The fit parameters are optimized to maximize the likelihood of a dataset [52]. The detailed procedure is included in the Supplemental Material [53]. An example dataset and the resulting probability distribution are shown in Fig. 4.

The constant k_θ can be calculated directly from the electrostatic fields:

$$k_\theta = \frac{1}{2}\frac{d^2}{dr^2}\int_{T_0}^{T_\mathrm{D}} \omega_r(r,t)dt\bigg|_{r=0}, \quad (3)$$

where T_0 is the time the cloud starts executing the gross magnetron orbit, and $T_\mathrm{D} = T_0 + 0.1\,\mathrm{s}$ is the time the cloud is released to the MCP. The frequency ω_r is time dependent because the trapping potential is morphed in preparation for

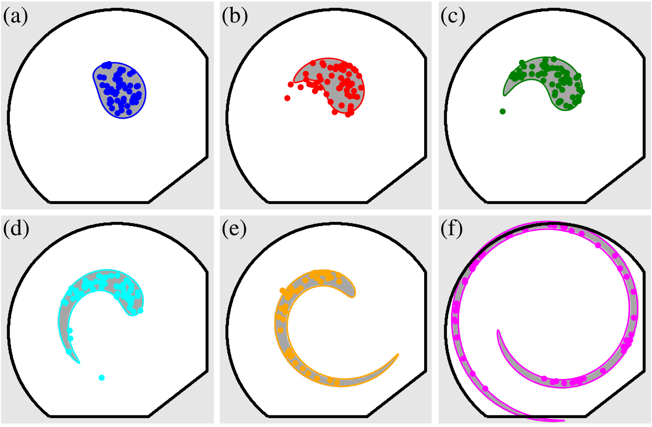

FIG. 4. A full dataset used to measure ε at one location in the trap. Each subplot shows 60 cloud center locations for one value of k_{2m}. The k_{2m} values are listed in the caption of Fig. 3. The shaded and outlined region is the 90% confidence interval of the probability distribution fit to all 360 datapoints.

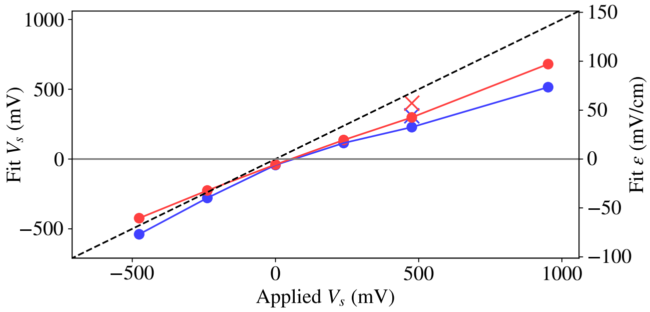

FIG. 5. The fit value of V_s (alternately, the on-axis electric field ε, where $\varepsilon = 0.211 V_s/R_w$) which best matches the experimental data versus the applied voltage V_s. For the crosses, the voltage was applied to the sector diametrically opposed to the one used for the rest of the data. The blue points are the fit results when using the leading order model for the displacement $\delta = \varepsilon/k_2$. The red points are the result of accounting for nonlinear corrections to the displacement. The dotted line delineates perfect agreement between fit V_s and applied V_s.

releasing the cloud. The calculated k_θ value can only be compared to those measured at the MCP by multiplying by a factor of $\mathcal{R}_B^2$. Thus, these values can be used to calibrate $\mathcal{R}_B$. The values of $\mathcal{R}_B$ we extract from different trap locations and different k_θ values typically vary by about 5%. If we average several datasets, we obtain $\mathcal{R}_B = 10.97$ with an error in the mean of 0.17, in agreement with calculations of the fields in the experimental apparatus. The magnetic field inside the trap is measured precisely [39], but the magnetic field at the MCP is influenced by the fringe fields of several magnets and some ferromagnetic material.

To benchmark our procedures and analysis, we performed the patch field measurement on a known, i.e. artificial, patch potential using an azimuthally sectored electrode (see Fig. 1). Potentials applied to such sectors have been used before [36,49,54,55] to move nonneutral plasmas off axis in Penning-Malmberg traps. Here, we applied a positive voltage V_e to five of the six azimuthal sectors of a sectored electrode to confine the cloud, and a perturbed voltage $V_e + V_s$ to the sixth sector to generate an artificial patch potential.

The results of the measurement of artificial patch potentials are shown in Fig. 5. The agreement with an electrostatic model is improved when we extend the previous linear model to include the nonlinear relationship between δ and $1/k_{2m}$ (see the Appendix). Note that the preexisting natural patch field, measured when $V_s = 0$, adds to the applied field. The component of the natural patch field parallel to the artificial one is inferred by changing which azimuthal segment V_s is applied to, reversing the electric field from the artificial patch. After accounting for nonlinearity and natural patch fields, the measured ε values are about 23% below our expectation. The known sources of error sum to less than 23%, as discussed in the Supplemental Material [53]. In the Appendix we suggest other effects that might explain this discrepancy. One of the primary physics goals of the ALPHA experiment is to measure the energy of the 1S–2S transition of antihydrogen. This measurement uses a 243 nm laser with approximately 1 W of circulating power in a Fabry-Pérot cavity [26,27]. While performing these measurements, we observed that several hours of exposure to ultraviolet laser light degrades the plasma trap—the expansion rate (and consequently the heating rate) of electron and positron plasmas increases. Without laser exposure, the trap can be operated for weeks without the heating rate increasing. For example, a plasma prepared using SDREVC [38] and cooled to 20 K by adiabatic expansion [56] rises to 40 K in 10 s before laser exposure, and to 400 K in 10 s after 6 h of laser exposure. Numerous authors have previously established that asymmetric electric fields cause plasma expansion, which converts electrostatic potential energy into heat, thereby raising the plasma temperatures [30,57–66]. Since increased plasma temperatures decrease the number of trapped antiatoms, it is fortunate that the trap's performance can be restored by letting the liquid helium that maintains the trap's 4 K electrodes evaporate, warming to room temperature, then recooling.

Figure 6 shows measured ε values before laser exposure, after 2.5 h of 1 W laser exposure, and after the trap was thermally cycled. Further, Fig. 7 illustrates how higher ε values after laser exposure are evident in cloud displacements. The magnitude of the patch field is increased by laser exposure, but thermally cycling the trap restores patch fields to their original values. This seems to indicate the presence of two kinds of patch potentials: one being an unchanging property of the

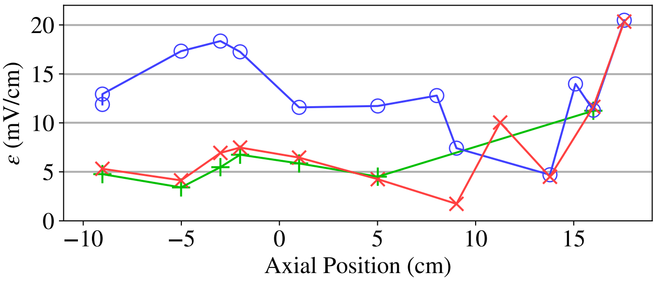

FIG. 6. The measured patch field ε as a function of axial position in the trap before laser exposure (+), after laser exposure (◯), and after a trap warming/cooling cycle (×). The horizontal axis is referenced to the ±14 cm marks in Fig. 1.

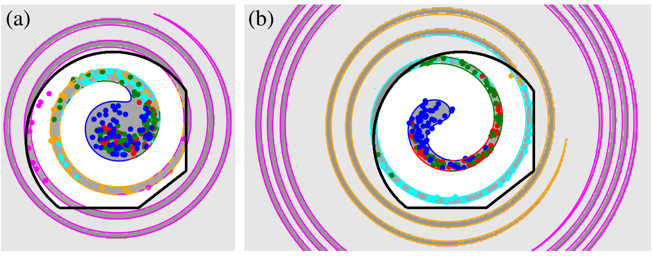

FIG. 7. Fit probability distributions (a) before and (b) after laser exposure. These figures are analogous to Fig. 4 if all six datasets shown there were plotted together along with the union of the six 90% confidence intervals. The edge of the confidence interval is colored according to which k_{2m} value is close to that part of the probability distribution.

electrode surface, and a second induced by lasers which only persists on a cold surface. Reference [6] hints at the possibility of static charges resting on layers of cryopumped gas. Laser light has previously been observed to induce patch potentials in planar ion traps [7] and single-particle Penning traps [22].

During measurements of antihydrogen's 1S–2S absorption spectrum, antiatoms in the 2S state ionize by absorbing an additional photon, ultimately leading to antiproton annihilation events on the trap wall. This paper shows that there are patch fields of sufficient magnitude to cause the antiprotons to travel to the trap wall in a time consistent with our observations. In ALPHA's most recent spectral measurements of antihydrogen, we quickly scan the laser frequency and rely on fast antiproton loss to confidently identify an annihilation event with the currently applied laser frequency. This way, an entire spectrum can be collected from multiple quick laser scans over one sample of antiatoms, reducing the data collection time from weeks to days.

In conclusion, a new *in situ* technique allows us to measure the magnitude of on-axis transverse electric fields. It is expected to be accurate to about 10%—the known sources of error are listed in the Supplemental Material [53]. Further investigation is required to resolve a 23% discrepancy in a controlled experiment where an artificially applied patch potential was measured. However, we believe this is most likely an issue that is unique to the artificial patch potential or a global calibration factor. The measurement can be used to monitor the buildup of patch potentials caused by laser light. The technique relies on the reproducible $\mathbf{E} \times \mathbf{B}$ drift motion of small electron clouds; these clouds may be useful for other kinds of measurements in Penning-Malmberg traps in the future.

This work was supported by: CNPq, FAPERJ, RENAFAE (Brazil); NSERC, NRC/TRIUMF, EHPDS/EHDRS, FQRNT (Canada); FNU (NICE Centre), Carlsberg Foundation (Denmark); ISF (Israel); STFC, EPSRC (UK); DOE, NSF (USA); and VR (Sweden).

Appendix on errors in the artificial patch field measurement. During measurements of the artificial patch field, the cloud's image charge is negligible, so the displacement δ only depends on V_s through the ratio V_s/V_e. To linear order, $\delta = \varepsilon/k_2 = (CV_s/V_e)R_w$, where $C \approx 0.311$ in this geometry (derived in the Supplemental Material [53]).

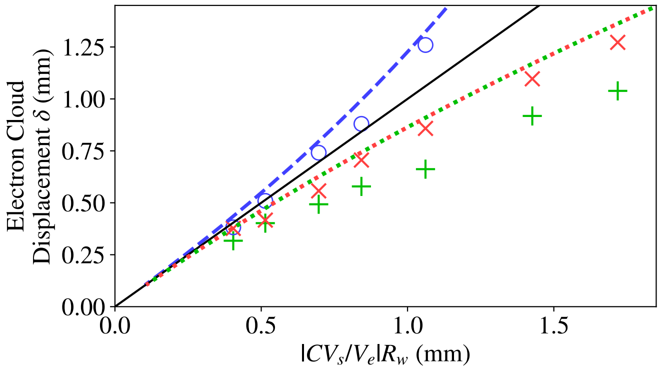

FIG. 8. A comparison between the linear relationship $\delta = \varepsilon/k_{2m} = (CV_s/V_e)R_w$, the nonlinear relationship $\delta = f(V_s/V_e)R_w$, and the measured data from three different artificial patch field measurements: $V_s = -476$ mV (○), $V_s = +476$ mV (+), and $V_s = +476$ mV applied to the diametrically opposed sector (×). In each of the three measurements, V_e is varied, and the ordinates of each point are the mean displacement of forty clouds. The solid black line is the linear theory. The blue dashed line is the nonlinear prediction $\delta = f(V_s/V_e)R_w$ where $V_s/V_e < 0$. The red and green dotted line corresponds to $V_s/V_e > 0$.

Aperturing and magnetic field line expansion limit the displacement of the clouds we can image to $\delta/R_w \lesssim 0.16 \ll 1$. Thus, one might expect that the linear order prediction for δ above would suffice. Experimentally, however, this prediction is inaccurate by about 50% for the artificial patches. Hence, we generalize to $\delta = f(V_s/V_e)R_w$, where f is the normalized exact location of the potential energy maximum; some properties of $f(V_s/V_e)$ are discussed in the Supplemental Material [53].

Agreement with the linear theory is generally better for natural patch potential measurements. In the Supplemental Material [53], it is shown that the artificial patch potential's geometry generates unusually significant nonlinearity; random voltage perturbations typically exhibit about three times less nonlinearity. Further, most of the natural patch potential measurements took place in a trap region where the wall radius was about 50% bigger than the trap region used for the artificial patch (see Fig. 1). Simple scaling shows that the larger radius suppresses nonlinearities by an additional factor of 1.5.

To test the nonlinear model, the assumption $\delta = \varepsilon/k_{2m}$ was replaced by $\delta = f(V_s/V_e)R_w$ in the probability distribution fit to the data, where f is calculated using electrostatic modeling of this particular sectored electrode. Figure 5 shows the measured patch fields using both models.

We also directly compare predicted and measured δ values by finding the mean distance between each cloud's position on the MCP and the position on the MCP which corresponds to the center of the trap (a parameter of the probability distribution fit). The results of this analysis are shown in Fig. 8. The data in this figure are extracted from three patch field measurements, one with positive V_s, one with negative V_s, and one with positive V_s applied to the diametrically opposed sector. In all three cases, observed δ values fall below the nonlinear prediction. Likewise, all three datasets result in a measurement of ε which is below the prediction.

One would expect that the component of the natural patch field parallel to the artificial patch field would increase δ when the artificial patch field is in one direction and decrease δ when the artificial patch field is flipped. Thus, the nonlinear prediction, the green and red dotted line in Fig. 8, should be between the observed δ values for the two opposing electrode segments.

After accounting for nonlinearity and the effect of natural patch fields, the measurements fall about 23% below our predictions. Known errors, listed in the Supplemental Material [53], add to about 10%. They do not entirely explain this discrepancy, but the following three speculative ideas might. Back of the envelope calculations and numeric simulations suggest that electrons moving between the electrodes and the MCP follow magnetic field lines nearly perfectly. Those field lines expand by a factor of $\mathcal{R}_B$, and the disagreement could be explained by $\mathcal{R}_B$ being 23% lower than the value extracted from k_θ values. However, this implies the magnetic field magnitude at the MCP is 50% above what modeling of the magnetic field suggests, which is unlikely. Second, an unknown electronics mistake which produces a voltage-divider-like decrease of V_s could explain the discrepancy; the experiment has remained operational for years and is never sufficiently disassembled such that V_s could be directly measured on the electrode surface. Finally, the sectored electrode used to create the artificial patch potential is also used to expand and compress nonneutral plasmas. This commonly leads to electrons, positrons, and antiprotons striking the trap wall. Like the scattered laser beam, this may change patch potentials, but the loss of charge might be azimuthally symmetric. This would change the potential on the surface of the electrode, effectively shifting V_e, without creating a significant on-axis electric field ε. This is a particular example of a more general possible issue: the natural patch potentials in this location might provide an unusually large contribution to the nonlinearity in δ. Further experiments will be needed to improve our understanding of this issue.

[1] C. Herring and M. H. Nichols, Thermionic emission, Rev. Mod. Phys. **21**, 185 (1949).

[2] J. B. Camp, T. W. Darling, and R. E. Brown, Macroscopic variations of surface potentials of conductors, J. Appl. Phys. **69**, 7126 (1991).

[3] M. Nonnenmacher, M. P. O'Boyle, and H. K. Wickramasinghe, Kelvin probe force microscopy, Appl. Phys. Lett. **58**, 2921 (1991).

[4] N. Gaillard, M. Gros-Jean, D. Mariolle, F. Bertin, and A. Bsiesy, Method to assess the grain crystallographic orientation with a submicronic spatial resolution using kelvin probe force microscope, Appl. Phys. Lett. **89**, 154101 (2006).

[5] C. D. Fosco, F. C. Lombardo, and F. D. Mazzitelli, Electrostatic interaction due to patch potentials on smooth conducting surfaces, Phys. Rev. A **88**, 062501 (2013).

[6] C. Benvenuti and N. Hilleret, Cold bore experiments at CERN ISR, Nuclear Science **26**, 4086 (1979).

[7] M. Harlander, M. Brownnutt, W. Hänsel, and R. Blatt, Trapped-ion probing of light-induced charging effects on dielectrics, New J. Phys. **12**, 093035 (2010).

[8] K. Li, H. Yin, C. Song, M. Hu, S. Wang, P. Luo, and Z. Zhou, Precision improvement of patch potential measurement in a scanning probe equipped torsion pendulum, Rev. Sci. Instrum. **93**, 065110 (2022).

[9] W. J. Weber, L. Carbone, A. Cavalleri, R. Dolesi, C. D. Hoyle, M. Hueller, and S. Vitale, Possibilities for measurement and compensation of stray dc electric fields acting on drag-free test masses, Adv. Space Res. **39**, 213 (2007).

[10] M. Armano, H. Audley, G. Auger, J. T. Baird, P. Binetruy, M. Born, D. Bortoluzzi, N. Brandt, A. Bursi, M. Caleno, A. Cavalleri, A. Cesarini, M. Cruise, K. Danzmann, M. de Deus Silva, I. Diepholz, R. Dolesi, N. Dunbar, L. Ferraioli, V. Ferroni *et al.*, and P. Zweifel (LISA Pathfinder Collaboration), Charge-induced force noise on free-falling test masses: Results from LISA pathfinder, Phys. Rev. Lett. **118**, 171101 (2017).

[11] S. Buchman and J. P. Turneaure, The effects of patch-potentials on the gravity probe B gyroscopes, Rev. Sci. Instrum. **82**, 074502 (2011).

[12] J. L. Garrett, J. Kim, and J. N. Munday, Measuring the effect of electrostatic patch potentials in Casimir force experiments, Phys. Rev. Res. **2**, 023355 (2020).

[13] S. E. Pollack, S. Schlamminger, and J. H. Gundlach, Temporal extent of surface potentials between closely spaced metals, Phys. Rev. Lett. **101**, 071101 (2008).

[14] R. O. Behunin, D. A. R. Dalvit, R. S. Decca, and C. C. Speake, Limits on the accuracy of force sensing at short separations due to patch potentials, Phys. Rev. D **89**, 051301(R) (2014).

[15] J. L. Garrett, D. Somers, and J. N. Munday, The effect of patch potentials in Casimir force measurements determined by heterodyne kelvin probe force microscopy, J. Phys.: Condens. Matter **27**, 214012 (2015).

[16] J. Xu, G. L. Klimchitskaya, V. M. Mostepanenko, and U. Mohideen, Reducing detrimental electrostatic effects in Casimir-force measurements and Casimir-force-based microdevices, Phys. Rev. A **97**, 032501 (2018).

[17] T. W. Darling, F. Rossi, G. I. Opat, and G. F. Moorhead, The fall of charged particles under gravity: A study of experimental problems, Rev. Mod. Phys. **64**, 237 (1992).

[18] G. Testera, The role of the patch effect electric fields in the penning trap method of measuring the gravitational force on antiprotons, Hyperfine Interact. **109**, 333 (1997).

[19] F. Rossi and G. I. Opat, Observations of the effects of adsorbates on patch potentials, J. Phys. D **25**, 1349 (1992).

[20] D. J. Berkeland, J. D. Miller, J. C. Bergquist, W. M. Itano, and D. J. Wineland, Minimization of ion micromotion in a paul trap, J. Appl. Phys. **83**, 5025 (1998).

[21] F. Heiße, S. Rau, F. Köhler-Langes, W. Quint, G. Werth, S. Sturm, and K. Blaum, High-precision mass spectrometer for light ions, Phys. Rev. A **100**, 022518 (2019).

[22] M. Bohman, Sympathetic cooling of a proton with resonant image current coupling, Ph.D. thesis, Heidelberg University (2020).

[23] D. E. Pritchard, Cooling neutral atoms in a magnetic trap for precision spectroscopy, Phys. Rev. Lett. **51**, 1336 (1983).

[24] G. B. Andresen, M. D. Ashkezari, M. Baquero-Ruiz, W. Bertsche, P. D. Bowe, E. Butler, C. L. Cesar, S. Chapman, M. Charlton, A. Deller, S. Eriksson, J. Fajans, T. Friesen, M. C. Fujiwara, D. R. Gill, A. Gutierrez, J. S. Hangst, W. N. Hardy, M. E. Hayden, A. J. Humphries *et al.*, Trapped antihydrogen, Nature (London) **468**, 673 EP (2010).

[25] J. Fajans and A. Schmidt, Malmberg-penning and minimum-B trap compatibility: The advantages of higher-order multipole traps, Nucl. Instrum. Methods Phys. Res. Sect. A **521**, 318 (2004).

[26] M. Ahmadi, B. X. R. Alves, C. J. Baker, W. Bertsche, E. Butler, A. Capra, C. Carruth, C. L. Cesar, M. Charlton, S. Cohen, R. Collister, S. Eriksson, A. Evans, N. Evetts, J. Fajans, T. Friesen, M. C. Fujiwara, D. R. Gill, A. Gutierrez, J. S. Hangst *et al.*, Observation of the 1S-2S transition in trapped antihydrogen, Nature (London) **541**, 506 (2017).

[27] M. Ahmadi, B. X. R. Alves, C. J. Baker, W. Bertsche, A. Capra, C. Carruth, C. L. Cesar, M. Charlton, S. Cohen, R. Collister, S. Eriksson, A. Evans, N. Evetts, J. Fajans, T. Friesen, M. C. Fujiwara, D. R. Gill, J. S. Hangst, W. N. Hardy, M. E. Hayden *et al.*, Characterization of the 1S-2S transition in antihydrogen, Nature (London) **557**, 71 (2018).

[28] C. Amole, G. B. Andresen, M. D. Ashkezari, M. Baquero-Ruiz, W. Bertsche, P. D. Bowe, E. Butler, A. Capra, P. T. Carpenter, C. L. Cesar, S. Chapman, M. Charlton, A. Deller, S. Eriksson, J. Escallier, J. Fajans, T. Friesen, M. C. Fujiwara, D. R. Gill, A. Gutierrez *et al.*, The alpha antihydrogen trapping apparatus, Nucl. Instrum. Methods Phys. Res. Sect. A **735**, 319 (2014).

[29] S. Sellner, M. Besirli, M. Bohman, M. J. Borchert, J. Harrington, T. Higuchi, A. Mooser, H. Nagahama, G. Schneider, C. Smorra, T. Tanaka, K. Blaum, Y. Matsuda, C. Ospelkaus, W. Quint, J. Walz, Y. Yamazaki, and S. Ulmer, Improved limit on the directly measured antiproton lifetime, New J. Phys. **19**, 083023 (2017).

[30] S. Robertson, Z. Sternovsky, and B. Walch, Reduction of asymmetry transport in the annular penning trap, Phys. Plasmas **11**, 1753 (2004).

[31] J. B. Camp, T. W. Darling, and R. E. Brown, Effect of crystallites on surface potential variations of Au and graphite, J. Appl. Phys. **71**, 783 (1992).

[32] D. A. Hite, K. S. McKay, and D. P. Pappas, Surface science motivated by heating of trapped ions from the quantum ground state, New J. Phys. **23**, 103028 (2021).

[33] J. Notte, A. J. Peurrung, J. Fajans, R. Chu, and J. S. Wurtele, Asymmetric stable equilibria of non-neutral plasmas, Phys. Rev. Lett. **69**, 3056 (1992).

[34] J. Fajans, E. Gilson, and E. Y. Backhaus, Bifurcations in elliptical, asymmetric non-neutral plasmas, Phys. Plasmas **7**, 3929 (2000).

[35] N. C. Hurst, J. R. Danielson, C. J. Baker, and C. M. Surko, Electron plasma orbits from competing diocotron drifts, Phys. Rev. Lett. **113**, 025004 (2014).

[36] T. Mortensen, A. Deller, C. A. Isaac, D. P. van der Werf, M. Charlton, and J. R. Machacek, Manipulation of the magnetron orbit of a positron cloud in a penning trap, Phys. Plasmas **20**, 012124 (2013).

[37] T. M. O'Neil and R. A. Smith, Stability theorem for off-axis states of a nonneutral plasma column, Physics of Fluids B: Plasma Physics **4**, 2720 (1992).

[38] M. Ahmadi, B. X. R. Alves, C. J. Baker, W. Bertsche, A. Capra, C. Carruth, C. L. Cesar, M. Charlton, S. Cohen, R. Collister, S. Eriksson, A. Evans, N. Evetts, J. Fajans, T. Friesen, M. C. Fujiwara, D. R. Gill, J. S. Hangst, W. N. Hardy, M. E. Hayden *et al.* (ALPHA Collaboration), Enhanced control and reproducibility of nonneutral plasmas, Phys. Rev. Lett. **120**, 025001 (2018).

[39] E. D. Hunter, A. Christensen, J. Fajans, T. Friesen, E. Kur, and J. S. Wurtele, Electron cyclotron resonance (ECR) magnetometry with a plasma reservoir, Phys. Plasmas **27**, 032106 (2020).

[40] J. R. Danielson, T. R. Weber, and C. M. Surko, Extraction of small-diameter beams from single-component plasmas, Appl. Phys. Lett. **90**, 081503 (2007).

[41] C. Smorra *et al.*, A reservoir trap for antiprotons, Int. J. Mass Spectrom. **389**, 10 (2015).

[42] S. A. Prasad and T. M. O'Neil, Finite length thermal equilibria of a pure electron plasma column, Phys. Fluids **22**, 278 (1979).

[43] A. J. Peurrung and J. Fajans, Non-neutral plasma shapes and edge profiles, Phys. Fluids B **2**, 693 (1990).

[44] R. L. Spencer, S. N. Rasband, and R. R. Vanfleet, Numerical calculation of axisymmetric non-neutral plasma equilibria, Phys. Fluids B **5**, 4267 (1993).

[45] A. J. Peurrung and J. Fajans, A limitation to the analogy between pure electron plasmas and two-dimensional inviscid fluids, Phys. Fluids B **5**, 4295 (1993).

[46] D. L. Eggleston, Electron vortex dynamics in an applied shear flow, AIP Conf. Proc. **331**, 54 (1995).

[47] F. F. Chen, *Introduction to Plasma Physics and Controlled Fusion*, 3rd ed. (Springer, Cham, 1984), Vol. 1.

[48] R. Chu, J. S. Wurtele, J. Notte, A. J. Peurrung, and J. Fajans, Pure electron plasmas in asymmetric traps*, Phys. Fluids B **5**, 2378 (1993).

[49] J. Notte, J. Fajans, R. Chu, and J. S. Wurtele, Experimental breaking of an adiabatic invariant, Phys. Rev. Lett. **70**, 3900 (1993).

[50] A. T. Rezakhani, A. K. Pimachev, and D. A. Lidar, Accuracy versus run time in an adiabatic quantum search, Phys. Rev. A **82**, 052305 (2010).

[51] N. C. Hurst, J. R. Danielson, D. H. E. Dubin, and C. M. Surko, Adiabatic behavior of an elliptical vortex in a time-dependent external strain flow, Phys. Rev. Fluids **6**, 054703 (2021).

[52] R. J. Rossi, *Mathematical statistics: An introduction to the likelihood based inference* (Wiley, New York, 2018); Int. Stat. Rev. **87**, 179 (2019).

[53] See Supplemental Material at http://link.aps.org/supplemental/10.1103/PhysRevResearch.6.L012008 for description of known sources of error for the models used in this paper, and a more detailed description of the fitting procedure [67–71].

[54] J. Notte, The effect of asymmetries on nonneutral plasmas, Ph.D. thesis, University of California, Berkeley (1993).

[55] J. Fajans, E. Gilson, and L. Friedland, Autoresonant (nonstationary) excitation of the diocotron mode in non-neutral plasmas, Phys. Rev. Lett. **82**, 4444 (1999).

[56] A. W. Hyatt, C. F. Driscoll, and J. H. Malmberg, Measurement of the anisotropic temperature relaxation rate in a pure electron plasma, Phys. Rev. Lett. **59**, 2975 (1987).

[57] J. H. Malmberg and C. F. Driscoll, Long-time containment of a pure electron plasma, Phys. Rev. Lett. **44**, 654 (1980).

[58] C. F. Driscoll and J. H. Malmberg, Length-dependent containment of a pure electron-plasma column, Phys. Rev. Lett. **50**, 167 (1983).

[59] R. Keinigs, Field-error induced transport in a pure electron plasma column, Phys. Fluids **27**, 1427 (1984).

[60] C. F. Driscoll, K. S. Fine, and J. H. Malmberg, Reduction of radial losses in a pure electron plasma, Phys. Fluids **29**, 2015 (1986).

[61] J. Notte and J. Fajans, The effect of asymmetries on non-neutral plasma confinement time, Phys. Plasmas **1**, 1123 (1994).

[62] D. L. Eggleston, Confinement of test particles in a malmberg–penning trap with a biased axial wire, Phys. Plasmas **4**, 1196 (1997).

[63] E. Y. Backhaus, J. Fajans, and J. S. Wurtele, Stability of highly asymmetric non-neutral plasmas, Phys. Plasmas **6**, 19 (1999).

[64] D. L. Eggleston and T. M. O'Neil, Theory of asymmetry-induced transport in a non-neutral plasma, Phys. Plasmas **6**, 2699 (1999).

[65] J. M. Kriesel and C. F. Driscoll, Two regimes of asymmetry-induced transport in non-neutral plasmas, Phys. Rev. Lett. **85**, 2510 (2000).

[66] Q. Quraishi, S. Robertson, and B. Walch, Electron diffusion in the annular penning trap, Phys. Plasmas **9**, 3264 (2002).

[67] D. H. E. Dubin, Cyclotron waves in a non-neutral plasma column, Phys. Plasmas **20**, 042120 (2013).

[68] R. D. Cousins, Why isn't every physicist a bayesian? Am. J. Phys. **63**, 398 (1995).

[69] R. Dubessy, T. Coudreau, and L. Guidoni, Electric field noise above surfaces: A model for heating-rate scaling law in ion traps, Phys. Rev. A **80**, 031402(R) (2009).

[70] M. S. Rzchowski and J. R. Henderson, Properties of random fields outside a metal surface and their effect on time-of-flight spectroscopy, Phys. Rev. A **38**, 4622 (1988).

[71] D. L. Eggleston, C. F. Driscoll, B. R. Beck, A. W. Hyatt, and J. H. Malmberg, Parallel energy analyzer for pure electron plasma devices, Phys. Fluids B **4**, 3432 (1992).